Computer-Assisted Screw Size and Insertion Trajectory Planning for Pedicle Screw Placement Surgery

Dejan Knez*, Boštjan Likar, Franjo Pernuš, and Tomaž Vrtovec

***Abstract*—Pathological conditions that cause instability of the spine are commonly treated by vertebral fixation involving pedicle screw placement surgery. However, existing methods for preoperative planning are based only on geometrical properties of vertebral structures (i.e., shape) without taking into account their structural properties (i.e., appearance). We propose a novel automated method for computer-assisted preoperative planning of the thoracic pedicle screw size and insertion trajectory. The proposed method extracts geometrical properties of vertebral structures by parametric modeling of vertebral bodies and pedicles in three dimensions (3D), and combines them with structural properties, evaluated through underlying image intensities in computed tomography (CT) images while considering the guidelines for pedicle screw design. The method was evaluated on 81 pedicles, obtained from 3D CT images of 11 patients that were appointed for pedicle screw placement surgery. In terms of mean absolute difference (MAD) and corresponding standard deviation (SD), the resulting high modeling accuracy of 0.39 ± 0.31 mm for 3D vertebral body models and 0.31 ± 0.25 mm for 3D pedicle models created an adequate anatomical frame for 3D pedicle screw models. When comparing the automatically obtained and manually defined plans for pedicle screw placement, a relatively high agreement was observed, with MAD $\pm$ SD of 0.4 ± 0.4 mm for the screw diameter, 5.8 ± 4.2 mm for the screw length, 2.0 ± 1.4 mm for the pedicle crossing point and $7.6 \pm 5.8°$ for screw insertion angles. However, a statistically significant increase of $48 \pm 26\%$ in the screw fastening strength in favor of the proposed automated method was observed in 99% of the cases.**

***Index Terms*—Pedicle modeling in 3D, pedicle morphometry, pedicle screw placement, preoperative planning, vertebral morphometry.**

I. Introduction

VERTEBRAL fixation is a surgical procedure for treating pathological conditions of the spine such as scoliosis, kyphosis, spondylolisthesis, spondlyosis, degenerative disease and herniation of the intervertebral disc, spinal tumors and vertebral fractures, as well as other conditions that cause instability of the spine [1]–[4]. As spinal instability may cause damage to the spinal cord and nerve roots, the aim of vertebral fixation is to reduce spinal mobility and, as a result, avoid such damage. The vertebral fixation procedure is based on anchoring two (or more) vertebrae to each other by metal fixation devices such as rods, plates and screws, and is therefore often termed as vertebral or spinal fusion. One of the most widely used fixation techniques is pedicle screw placement [5], which consists of inserting screws through vertebral pedicles from the posterior side into the interior of the vertebral body, and then attaching stabilizing rods to hooks on the exterior part of the screws. The procedure is considered complex and technically demanding with a steep learning curve [6], as there is limited visibility of critical anatomical structures during surgery. As a result, it is important that the surgeon gains a mental conceptualization and reconstruction of the three-dimensional (3D) anatomy of spinal structures that are hidden from direct view. Although pedicles are, from the biomechanical point of view, the hardest part of a vertebra, their narrow anatomical shape poses a risk of injury to the spinal cord, nerve roots and aorta if pedicle wall breakthrough or other damage in the case of pedicle screw misplacement occur. For a safe pedicle screw placement, the surgeon has to perform proper surgery planning by taking into account pedicle morphometry, and choosing the appropriate size and insertion trajectory of each pedicle screw, which proved valuable for reducing the risk of screw misplacement [7]. Therefore, image-guided and navigation techniques have been widely used to improve the accuracy of pedicle screw placement [8], [9] by intraoperatively tracking surgical instruments and providing the surgeon with their current position in images of the treated patient [10]. The quality of the alignment between the 3D preoperative image and two-dimensional (2D) intraoperative images is evaluated by the accuracy of the corresponding 3D/2D registration [10], usually specified as the mean target registration error (mTRE) [8], [10]. For pedicle screw placement surgery, a mTRE of up to 2 mm is considered to be clinically acceptable [8], while screw translation and rotation of up to 1 mm and 5°, respectively, are considered to be the allowable margins of error [11] that, however, decrease with larger pedicle screws planned for the same pedicle dimensions. In addition, one of the most widely accepted grading methods for assessing pedicle screw placement accuracy is based on evaluating pedicle wall breaches from computed tomography

Manuscript received November 12, 2015; revised December 21, 2015; accepted December 29, 2015. Date of publication January 05, 2016; date of current version May 28, 2016. This work has been supported by the Slovenian Research Agency under grants P2-0232, J2-5473, J7-6781, and J2-7118. *Asterisk indicates corresponding author.*

*D. Knez is with the Laboratory of Imaging Technologies, Faculty of Electrical Engineering, University of Ljubljana, SI-1000 Ljubljana, Slovenia (e-mail: dejan.knez@fe.uni-lj.si).

B. Likar, F. Pernuš, and T. Vrtovec are with the Laboratory of Imaging Technologies, Faculty of Electrical Engineering, University of Ljubljana, SI-1000 Ljubljana, Slovenia (e-mail: bostjan.likar@fe.uni-lj.si; franjo.pernus@fe.uni-lj.si; tomaz.vrtovec@fe.uni-lj.si).

Color versions of one or more of the figures in this paper are available online at http://ieeexplore.ieee.org.

Digital Object Identifier 10.1109/TMI.2016.2514530

(CT) scans by classifying them into 2 mm incremental steps, and considering screws with breaches of up to 2 mm as the acceptable safe zone [12].

Besides intraoperatively tracking of surgical instruments, image-guided and navigation techniques enable intraoperative transfer of a preoperatively defined pedicle screw placement plan. Preoperative planning has therefore become essential for a safe and reliable pedicle screw placement surgery. During planning, the surgeon studies in detail the spinal anatomy of the treated patient by relying on preoperative images, which are in the case of spine surgery nowadays usually in the form of 3D CT scans. Modern visualization software allows the surgeon to prepare the operative plan by manually navigating through the 3D image and manipulating with 3D vertebra and 3D pedicle screw models, which is however time-consuming even for a surgeon experienced with such software. What is more important is that such planning is also relatively unreliable due to the subjective interpretation of the surgeon and the fact that it is practically impossible to take into consideration all important parameters for pedicle screw placement, for example, the screw pull-out strength. To alleviate these problems, computer-assisted methods for pedicle screw size and insertion trajectory planning were proposed [13], [14], however, these methods are often based on 2D images and/or rely only on geometrical properties of vertebral structures (i.e., shape) without taking into account their structural properties (i.e., appearance), such as the bone mineral density (BMD). As the pedicle screw pull-out strength correlates with its underlying BMD [2], and vertebral body and pedicle morphology impose limitations to the pedicle screw size and insertion trajectory, both geometrical and structural properties of vertebrae have to be considered in planning of pedicle screw placement.

In this paper, we propose a novel, automated method for computer-assisted preoperative planning of the screw size and insertion trajectory for thoracic pedicle screw placement surgery. Geometrical properties of vertebral bodies and pedicles are extracted by parametric modeling in 3D, which enables direct measurements of vertebral and pedicle morphometry in 3D, as well as creating a proper anatomical frame for pedicle screw modeling. The optimal size and insertion trajectory of pedicle screws are then obtained from 3D pedicle screws models that are determined by combining geometrical properties of vertebral bodies and pedicles with their structural properties, evaluated through underlying image intensities in the observed CT images while considering the guidelines for pedicle screw design.

II. Methods

A. Modeling of Vertebral Structures in 3D

For the purpose of creating an appropriate anatomical frame for preoperative planning of pedicle screw placement procedures, we base vertebral body and pedicle modeling in 3D on superquadrics [15] that are defined by the inside-outside function:

$$M(\boldsymbol{x}) = \left(\left(\frac{x}{A_1} \right)^{2/\epsilon_2} + \left(\frac{y}{A_2} \right)^{2/\epsilon_2} \right)^{\epsilon_2/\epsilon_1} + \left(\frac{z}{A_3} \right)^{2/\epsilon_1}, \quad (1)$$

where an arbitrary point $\boldsymbol{x} = (x, y, z) \in \mathbb{R}^3$ in the 3D Cartesian space can be located inside ($M(\boldsymbol{x}) < 1$), outside ($M(\boldsymbol{x}) > 1$) or on the superquadric surface ($M(\boldsymbol{x}) = 1$). Parameters A_1, A_2 and A_3 define the size of the superquadric along coordinate axes x (left-to-right), y (anterior-to-posterior) and z (superior-to-inferior), respectively, and parameters ϵ_1 and ϵ_2 control the smoothness of the superquadric edge. Specific 3D shapes can be obtained by adding rigid or non-rigid deformations to $M(\boldsymbol{x})$ [16], which was already used for parametric modeling of vertebral bodies and intervertebral discs [17], [18]. In this work, we adapt the existing 3D model of the vertebral body [18] and develop a completely novel 3D model of the pedicle.

1) 3D Vertebral Body Model: The initial 3D model of the vertebral body $V_{init}(\boldsymbol{x})$ is represented with a superquadric $M(\boldsymbol{x})$ (1) forming an elliptical cylinder with $\epsilon_1 = 0.1$ and $\epsilon_2 = 1$:

$$V_{init}(\boldsymbol{x}) = \left(\frac{x^2 + y^2}{R_v(\theta)^2} \right)^{10} + \left(\frac{z}{H_v} \right)^{20}, \quad (2)$$

where H_v is its half-height, $R_v(\theta)$ is its radius with A_v being the semi-major and B_v the semi-minor axis of the ellipse, and $\theta = \arctan(y/x)$ is the radial angle in the xy-plane:

$$R_v(\theta) = \frac{A_v B_v}{\sqrt{(A_v \sin\theta)^2 + (B_v \cos\theta)^2}}. \quad (3)$$

A more detailed 3D model of the vertebral body $V_{def}(\boldsymbol{x})$ is obtained by adding specific deformations to $V_{init}(\boldsymbol{x})$. Four Gaussian functions with magnitude m and standard deviation σ at angular location φ deform the radius $R_v(\theta)$ into $R_G(\theta)$:

$$R_G(\theta) = R_v(\theta) \left(1 + \sum_{j \in \{l,r,f,a\}} m_j \mathrm{e}^{-(\theta - \varphi_j)^2 / 2\sigma_j^2} \right), \quad (4)$$

and model the location of the left pedicle (m_l, σ_l, φ_l), right pedicle (m_r, σ_r, φ_r), vertebral foramen (m_f, σ_f, φ_f) and anterior part of the vertebral body (m_a, σ_a, φ_a). The concavity of the vertebral body wall is modeled by two cosine functions of magnitude c_{wa} for the anterior part of the vertebral body and c_{wf} for the part around the vertebral foramen that are respectively regulated by rectangle functions Π centered at φ_a and φ_f with duration $3\pi/4$ and $\pi/4$, which deform the radius $R_G(\theta)$ along the longitudinal axis z of the cylinder into $R_C(z, \theta)$:

$$R_C(z,\theta) = R_G(\theta) \left(1 - \cos\left(\frac{\pi z}{H_v} \right) \cdot \left(c_{wa} \Pi\left(\frac{3\pi}{4}, \varphi_a \right) + c_{wf} \Pi\left(\frac{\pi}{4}, \varphi_f \right) \right) \right). \quad (5)$$

Concavities of vertebral endplates are modeled by two 2D cosine functions with period $R_C(z, \theta)$ and magnitude $c_e = c_{es}$ for the superior ($z \geq 0$) and $c_e = c_{ei}$ for the inferior endplate ($z < 0$), which deform the half-height H_v of the cylinder into $H_C(z, \theta)$:

$$H_C(z,\theta) = H_v \left(1 - c_e \cos\left(\frac{\pi \sqrt{x^2 + y^2}}{R_C(z,\theta)} \right) \right). \quad (6)$$

Inclinations of vertebral endplates are modeled by bending the superquadric with magnitude $s_e = s_{es}$ in the direction of angle $\psi_e = \psi_{es}$ for the superior ($z \geq 0$) and with magnitude $s_e = s_{ei}$ in the direction of angle $\psi_e = \psi_{ei}$ for the inferior endplate ($z < 0$):

$$\begin{pmatrix} x \\ y \\ z \end{pmatrix} = \begin{pmatrix} x + (b_R - b_r)\cos\psi_e \\ y + (b_R - b_r)\sin\psi_e \\ z + (s_e^{-1} - b_r)\sin(z s_e^{-1}) \end{pmatrix}, \tag{7}$$

where b_r is the projection of x and y components of superquadric surface points onto the bending plane, and b_R is the bending transformation of b_r:

$$\begin{aligned} b_r &= \sqrt{x^2 + y^2}\cos(\psi_e - \theta), \\ b_R &= s_e^{-1} - (s_e^{-1} - b_r)\cos(z s_e^{-1}). \end{aligned} \tag{8}$$

The increasing size and torsion of the vertebral body are modeled by linear transformations t_{vbs} and t_{vbt}, respectively, that deform the radius $R_C(z,\theta)$ and the radial angle θ along axis z of the cylinder into $R_S(z,\theta)$ and $\theta_T(z,\theta)$, respectively:

$$\begin{aligned} R_S(z,\theta) &= R_C(z,\theta)\left(1 - t_{vbs}\frac{z}{H_v}\right), \\ \theta_T(z,\theta) &= \theta + t_{vbt}\frac{z}{H_v}. \end{aligned} \tag{9}$$

In total, 25 parameters are therefore used to obtain a detailed 3D model of the vertebral body $V_{def}(\boldsymbol{x})$, out of which three parameters [(2) and (3)] define the size of the initial elliptical cylinder $V_{init}(\boldsymbol{x})$, while 22 parameters [(4)–(9)] define transformation $\mathcal{T}_V$ that deforms $V_{init}(\boldsymbol{x})$ into $V_{def}(\boldsymbol{x}) = \mathcal{T}_V(V_{init}(\boldsymbol{x}))$. The pose of the 3D vertebral body model in the 3D image space is defined by its center point location $\boldsymbol{x}_v = (x_v, y_v, z_v)$ and rotation $\boldsymbol{\alpha}_v = (\alpha_v, \beta_v, \gamma_v)$ through rigid transformation $\mathcal{R}_V$ that transforms $V_{def}(\boldsymbol{x})$ into $V(\boldsymbol{x}) = \mathcal{R}_V\left(V_{def}(\boldsymbol{x})\right) = \mathcal{R}_V\left(\mathcal{T}_V\left(V_{init}(\boldsymbol{x})\right)\right)$.

2) 3D Pedicle Model: The initial 3D model of the pedicle $P_{init}(\boldsymbol{x})$ is also represented with a superquadric $M(\boldsymbol{x})$ (1) forming an elliptical cylinder (2), however, with edge smoothness parameters set to $\epsilon_1 = 0.01$ and $\epsilon_2 = 1$ corresponding to sharper edges:

$$P_{init}(\boldsymbol{x}) = \left(\frac{x^2 + z^2}{R_p(\vartheta)^2}\right)^{100} + \left(\frac{y}{L_p}\right)^{200}, \tag{10}$$

where L_p is its half-length, $R_p(\vartheta)$ is its radius with A_p being the semi-major and B_p the semi-minor axis of the ellipse, and $\vartheta = \arctan(z/x)$ is the radial angle in the xz-plane:

$$R_p(\vartheta) = \frac{A_p B_p}{\sqrt{(A_p\sin\vartheta)^2 + (B_p\cos\vartheta)^2}}. \tag{11}$$

A more detailed 3D model of the pedicle $P_{def}(\boldsymbol{x})$ is obtained by adding specific deformations to $P_{init}(\boldsymbol{x})$. The concavity of the pedicle wall is modeled by four cosine functions of magnitude w_s for the superior, w_i for the inferior, w_l for the left and w_r for the right part of the pedicle wall that are respectively regulated by rectangle functions Π centered at y_{ws}, y_{wi}, y_{wl} and y_{wr} with durations w_{ws}, w_{wi}, w_{wl} and w_{wr} (Fig. 1), which deform axes

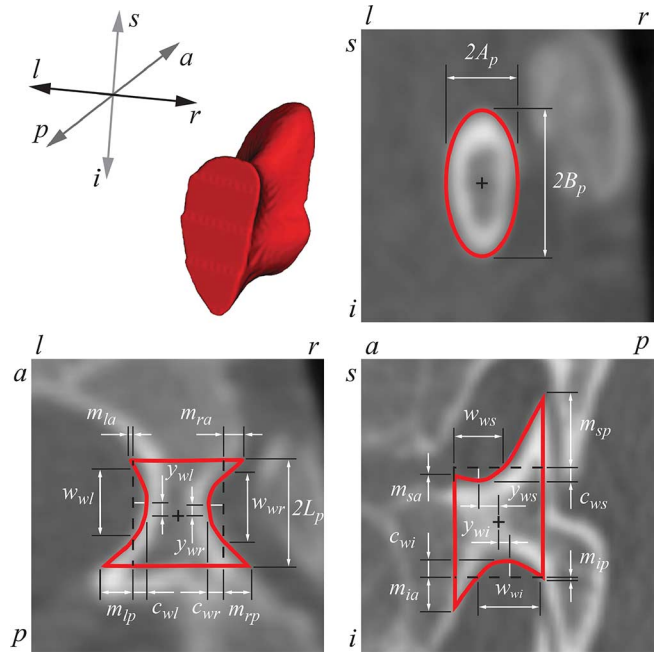

Fig. 1. The initial 3D pedicle model in the form of an elliptical cylinder (semi-major axis A_p, semi-minor axis B_p, half-length L_p) is deformed by the concavity of the pedicle wall at its superior (c_{ws}, y_{ws}, w_{ws}), inferior (c_{wi}, w_{ci}, w_{wi}), left (c_{wl}, y_{wl}, w_{wl}) and right (c_{wr}, y_{wr}, w_{wr}) part, and by the shape of pedicle tails at its superior-anterior/posterior (m_{sa} and m_{sp}), inferior-anterior/posterior (m_{ia} and m_{ip}), left-anterior/posterior (m_{la} and m_{lp}), and right-anterior/posterior (m_{ra} and m_{rp}) part. (l-left, r-right, a-anterior, p-posterior, s-superior, i-inferior).

A_p and B_p of the ellipse along the longitudinal axis y of the cylinder into $A_C(y,\vartheta)$ and $B_C(y,\vartheta)$, respectively:

$$\begin{aligned} A_C(y,\vartheta) &= A_p \sum_{j\in\{s,i\}} 1_j(\vartheta) c_{wj} \\ &\quad \cdot \cos\left(\frac{\pi}{2}\frac{y - y_{wj}}{w_{wj}}\right)\Pi\left(w_{wj}, y_{wj}\right), \\ B_C(y,\vartheta) &= B_p \sum_{j\in\{l,r\}} 1_j(\vartheta) c_{wj} \\ &\quad \cdot \cos\left(\frac{\pi}{2}\frac{y - y_{wj}}{w_{wj}}\right)\Pi\left(w_{wj}, y_{wj}\right), \end{aligned} \tag{12}$$

where $1_j(\vartheta) \in \{0,1\}$ is the indicator function that limits the radial angle ϑ and defines the observed part of the pedicle wall by equaling 1 only when $j = s$ and $-\pi/2 < \vartheta \leq \pi/2$ (superior part), $j = i$ and $\pi/2 < \vartheta \leq 3\pi/2$ (inferior part), $j = l$ and $0 < \vartheta \leq \pi$ (left part), and $j = r$ and $\pi < \vartheta \leq 2\pi$ (right part). Eight Gaussian functions with magnitude m and standard deviation $L_p/2$ at longitudinal location y_k deform the semi-major axis $A_C(y,\vartheta)$ and the semi-minor axis $B_C(y,\vartheta)$ of the ellipse into $A_G(y,\vartheta)$ and $B_G(y,\vartheta)$, respectively:

$$\begin{aligned} A_G(y,\vartheta) &= A_C(y,\vartheta) \sum_{j\in\{s,i\}} \sum_{k\in\{a,p\}} m_{jk} \mathrm{e}^{-(y-y_k)^2/(L_p^2/2)}, \\ B_G(y,\vartheta) &= B_C(y,\vartheta) \sum_{j\in\{l,r\}} \sum_{k\in\{a,p\}} m_{jk} \mathrm{e}^{-(y-y_k)^2/(L_p^2/2)}, \end{aligned} \tag{13}$$

and model pedicle tails at the superior-anterior/posterior (m_{sa} and m_{sp}) and inferior-anterior/posterior (m_{ia} and m_{ip}) part of

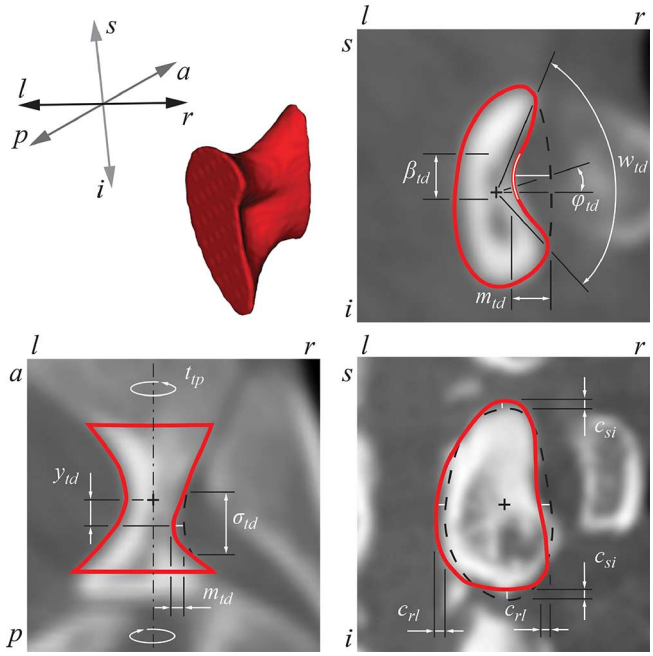

Fig. 2. The 3D pedicle model from Fig. 1 is further deformed by the teardrop shape ($m_{td}, w_{td}, \beta_{td}, \varphi_{td}, \sigma_{td}, y_{td}$), kidney shape ($c_{lr}, c_{si}$) and torsion ($t_{pt}$) of the pedicle. ($l$-left, r-right, a-anterior, p-posterior, s-superior, i-inferior).

the pedicle within $A_G(y,\vartheta)$, and at the left-anterior/posterior (m_{la} and m_{lp}) and right-anterior/posterior (m_{ra} and m_{rp}) part of the pedicle within $B_G(y,\vartheta)$, where $y_k = -L_p$ for the anterior ($k = a$) and $y_k = +L_p$ for the posterior ($k = p$) part of the pedicle (Fig. 1). The teardrop shape of the pedicle [19] is modeled by the Fermi-Dirac function [20] with magnitude m_{td}, shape parameter β_{td} and width w_{td} at angular location φ_{td}, which is regulated by a Gaussian function with standard deviation σ_{td} at location y_{td} and deforms the semi-minor axis $B_G(y,\vartheta)$ of the ellipse into $B_{TD}(y,\vartheta)$ (Fig. 2):

$$B_{TD}(y,\vartheta) = B_G(y,\vartheta)\frac{m_{td}}{1+\mathrm{e}^{\beta_{td}((|\vartheta-\varphi_{td}|/w_{td})-1)}}\mathrm{e}^{-(y-y_{td})^2/2\sigma_{td}^2}. \quad (14)$$

The kidney shape of the pedicle [19] is modeled by two cosine functions of magnitudes c_{lr} and c_{si} with periods $2A_p$ and $2B_p$ for the deformation in the left-to-right and superior-to-inferior direction, respectively, which are regulated by rectangular functions Π centered at 0 with durations $2A_p$ and $2B_p$ (Fig. 2):

$$\begin{pmatrix} x \\ y \\ z \end{pmatrix} = \begin{pmatrix} c_{lr}\cos\left(\frac{\pi}{2}\frac{z}{2A_p}\right)\Pi\left(2A_p,0\right) \\ y \\ c_{si}\cos\left(\frac{\pi}{2}\frac{x}{2B_p}\right)\Pi\left(2B_p,0\right) \end{pmatrix}. \quad (15)$$

The torsion of the pedicle is modeled by the linear transformation t_{pt} that deforms the radial angle ϑ along axis y of the cylinder into $\vartheta_T(y,\vartheta)$:

$$\vartheta_T(y,\vartheta) = \vartheta + t_{pt}\frac{y}{L_p}. \quad (16)$$

In total, 32 parameters are therefore used to obtain a detailed 3D model of the pedicle $P_{def}(\boldsymbol{x})$, out of which three parameters [(10) and (11)] define the size of the initial elliptical cylinder $P_{init}(\boldsymbol{x})$, while 29 parameters [(12)–(16)] define transformation $\mathcal{T}_P$ that deforms $P_{init}(\boldsymbol{x})$ into $P_{def}(\boldsymbol{x}) = \mathcal{T}_P(P_{init}(\boldsymbol{x}))$. The pose of the 3D pedicle model in the 3D image space is defined by its center point location $\boldsymbol{x}_p = (x_p, y_p, z_p)$ and rotation $\boldsymbol{\alpha}_p = (\alpha_p, \beta_p, \gamma_p)$ through rigid transformation $\mathcal{R}_P$ that transforms $P_{def}(\boldsymbol{x})$ into $P(\boldsymbol{x}) = \mathcal{R}_P\left(P_{def}(\boldsymbol{x})\right) = \mathcal{R}_P\left(\mathcal{T}_P\left(P_{init}(\boldsymbol{x})\right)\right)$.

3) Alignment of 3D Vertebral Body and Pedicle Models to Anatomical Structures in CT Images: To align the generated 3D models of the vertebral body and pedicle to the observed vertebral structures in CT images, we evaluate the similarity between each 3D model and characteristic properties of CT images by criterion $\mathcal{S}$ [18]:

$$\mathcal{S} = \sqrt{1-\sum_s \sqrt{p_{ins}(s)p_{sur}(s)}} \cdot \sum_{\boldsymbol{x}\in\Lambda}\left(\left\langle \boldsymbol{g}(\boldsymbol{x}), \boldsymbol{n}(\boldsymbol{x})\right\rangle \mathrm{e}^{-d(\boldsymbol{x})^2/2\sigma_\Lambda^2}\right). \quad (17)$$

The image intensity component of $\mathcal{S}$ is defined with the Bhattacharyya distance [21] and used to maximize the amount of soft tissues in the surroundings of the 3D model and the amount of bone structures inside the 3D model, represented respectively by probability distributions $p_{sur}(s)$ and $p_{ins}(s)$ of intensity range s. The gradient component of $\mathcal{S}$ is used to maximize the agreement between image intensity gradients $\boldsymbol{g}(\boldsymbol{x})$ and corresponding 3D model normals $\boldsymbol{n}(\boldsymbol{x})$, where $d(\boldsymbol{x})$ is the Euclidean distance from point $\boldsymbol{x}$ to the corresponding point on the 3D model surface along its normal vector, Λ is the region within distance $d_\Lambda = \sqrt{A_v B_v}/H_v$ from the 3D model surface with standard deviation σ_Λ, and $\langle \boldsymbol{g}(\boldsymbol{x}), \boldsymbol{n}(\boldsymbol{x})\rangle$ is the dot product between image intensity gradient vector $\boldsymbol{g}(\boldsymbol{x})$ and outward-pointing normalized 3D model surface normal vector $\boldsymbol{n}(\boldsymbol{x})$ when their wrap-around angle is smaller than $\pi/2$. The final 3D models of the vertebral body $V(\boldsymbol{x})$ and pedicle $P(\boldsymbol{x})$ are therefore obtained by searching for parameters of composite transformations $\mathcal{R}_V \circ \mathcal{T}_V$ and $\mathcal{R}_P \circ \mathcal{T}_P$, respectively, that maximize the similarity $\mathcal{S}$:

$$\begin{pmatrix} \mathcal{R}_V \circ \mathcal{T}_V \\ \mathcal{R}_P \circ \mathcal{T}_P \end{pmatrix} = \arg\max_{\mathcal{R}\circ\mathcal{T}}\left(\mathcal{S}\Big|_{\mathcal{R},\mathcal{T}}\right), \quad (18)$$

where $\mathcal{T}$ is an arbitrary deformation and $\mathcal{R}$ is an arbitrary rigid transformation of the 3D vertebral body or pedicle model.

B. Modeling of Pedicle Screws in 3D

Although pedicle screws are manufactured in a variety of forms and types, can be slightly cone-shaped (i.e., pointed) and have different thread characteristics (e.g., pitch and angle), we generalize their 3D shape to a simple yet representative cylinder that is aligned to the observed vertebral bodies and pedicles in CT images.

1) 3D Pedicle Screw Model: The initial 3D model of the pedicle screw $S_{init}(\boldsymbol{x})$ is represented with a superquadric $M(\boldsymbol{x})$ (1) forming a circular cylinder with sharp edges ($\epsilon_1 = 0.01, \epsilon_2 = 1$):

$$S_{init}(\boldsymbol{x}) = \left(\frac{x^2+z^2}{R_s^2}\right)^{100} + \left(\frac{y}{L_s}\right)^{200}, \quad (19)$$

where L_s is its half-length and R_s is its radius in the xz-plane ($2R_s$ is the screw pitch diameter). A more detailed model of

the pedicle screw $S_{def}(\boldsymbol{x}) = \mathcal{T}_S(S_{init}(\boldsymbol{x}))$ is obtained by modifying L_s and R_s that define transformation $\mathcal{T}_S$. The pose of the 3D pedicle screw model in the 3D image space is defined by position $\boldsymbol{x}_s = (x_s, y_s, z_s)$ and rotation $\boldsymbol{\alpha}_s = (\alpha_s, \beta_s, \gamma_s)$ through rigid transformation $\mathcal{R}_S$ that transforms $S_{def}(\boldsymbol{x})$ into $S(\boldsymbol{x}) = \mathcal{R}_S\Big(S_{def}(\boldsymbol{x})\Big) = \mathcal{R}_S\Big(\mathcal{T}_S\big(S_{init}(\boldsymbol{x})\big)\Big)$.

2) Alignment of 3D Pedicle Screw Models to Anatomical Structures in CT Images: In planning of pedicle screw placement procedures, both geometrical (i.e., shape) and structural (i.e., appearance) properties of vertebrae have to be considered. The following conditions $\mathcal{C}$ related to the 3D pedicle screw model $S(\boldsymbol{x})$ are imposed to account for vertebral geometrical properties:

$\mathcal{C}_1$: $S(\boldsymbol{x})$ must be located within the 3D vertebral body model $V(\boldsymbol{x})$, therefore preventing eventual breakthroughs of the vertebral body wall that can result in injuries to the aorta and/or internal organs,

$\mathcal{C}_2$: $S(\boldsymbol{x})$ must be located within the 3D pedicle model $P'(\boldsymbol{x})$ (obtained by shrinking $P(\boldsymbol{x})$ for d_s, which represents the safety margin in the form of a constant distance between the surface of $P(\boldsymbol{x})$ and the surface of $P'(\boldsymbol{x})$), therefore preventing eventual breakthroughs of the pedicle wall as well as screw locations on the pedicle surface boundary that can result in injuries to the spinal cord and/or nerve roots, and

$\mathcal{C}_3$: $S(\boldsymbol{x})$ must not, within $V(\boldsymbol{x})$, cross the virtual yz-plane of vertebral symmetry in the left-to-right anatomical direction, obtained from $V(\boldsymbol{x})$, therefore preventing eventual intersections with the screw through the opposite pedicle.

To account for vertebral structural properties, we rely on biomechanical characteristics of the bone and fixation by screws. The screw pull-out strength has been recognized as the biomechanical parameter that should be optimized for the screw design [22], and it was shown that it is related to the underlying BMD [2]. For this purpose, the screw fastening strength [2], [23], which can be also termed as the screw fixation strength, was introduced as a measure of CT image intensities within the planned screw volume. These CT image intesities further correlate with BMD [24] and consequently with the screw pull-out strength. However, in practice surgeons first create a pilot hole for the screw before its actual placement [25], and therefore image intensities around the longitudinal screw axis do not contribute to the fastening strength. As a result, we propose a modified version of the fastening strength F to account for vertebral structural properties:

$$F = \int_{-L_s}^{+L_s} \int_{0}^{2\pi} \int_{R_s-\Delta}^{R_s+\Delta} r I_w(r, \varphi, y) \mathrm{d}r \, \mathrm{d}\varphi \, \mathrm{d}y, \qquad (20)$$

where $I_w(\boldsymbol{r}) = I_w(r, \varphi, y)$ is the weighted 3D image intensity $I(\boldsymbol{r}) = I(r, \varphi, y)$ under cylindrical coordinates $\boldsymbol{r} = (r, \varphi, y) \in \mathbb{R}^3$, and 2Δ is the span around the screw thread between its minor radius $R_s - \Delta$ and major radius $R_s + \Delta$. By introducing Δ, only image intensities corresponding to the screw thread contribute to F. Besides applying the cut-off in the form of safety margin d_s (see condition $\mathcal{C}_2$), the trade-off between BMD of the cortical bone at the pedicle wall and BMD of the trabecular bone inside the pedicle is achieved by weighting 3D image intensities with a Gaussian function so that the influence of BMD decreases when moving from the longitudinal axis of the 3D pedicle model $P'(\boldsymbol{x})$ towards the pedicle wall:

$$I_w(\boldsymbol{r}) = I(\boldsymbol{r}) \mathrm{e}^{-2d(\boldsymbol{r})^2 / d_p(\boldsymbol{r})^2}, \qquad (21)$$

where $d(\boldsymbol{r})$ is the shortest distance from the longitudinal axis of $P'(\boldsymbol{x})$ to $\boldsymbol{r}$, while $d_p(\boldsymbol{r})$ is the distance from the longitudinal axis of $P'(\boldsymbol{x})$ to the 3D pedicle model surface point along the line that connects the longitudinal axis of $P'(\boldsymbol{x})$ with $\boldsymbol{r}$.

Both geometrical and structural properties of vertebrae are taken into account for the determination of the final 3D pedicle screw model $S(\boldsymbol{x})$, which is aligned to the observed vertebral body and observed pedicle in the 3D image by searching for parameters of the composite transformation $\mathcal{R}_S \circ \mathcal{T}_S$ that maximize the normalized fastening strength $\mathcal{F}$:

$$\mathcal{R}_S \circ \mathcal{T}_S = \arg\max_{\mathcal{R} \circ \mathcal{T}} \left(\mathcal{F} \Big|_{\mathcal{R}, \mathcal{T}, \mathcal{C}} \right); \quad \mathcal{F} = \frac{F}{8\pi R_s L_s \Delta}, \qquad (22)$$

where $8\pi R_s L_s \Delta$ is the normalization coefficient in the form of the screw thread volume, and $\mathcal{T}$ is an arbitrary deformation and $\mathcal{R}$ is an arbitrary rigid transformation of the 3D pedicle screw model. As F directly increases with increasing screw radius R_s and length $2L_s$, maximization of $\mathcal{F}$ instead of F does not favor larger and longer screws.

3) Planning of Pedicle Screw Size and Insertion Trajectory: From the final 3D pedicle screw model $S(\boldsymbol{x})$ that is aligned to the observed vertebral structures in CT images, we extract the following clinically relevant parameters:

1. The *pedicle screw size* reflects the shape of the screw in 3D and is represented by the screw major diameter $D = 2(R_s + \Delta)$ and screw length $L = 2L_s$, which are extracted directly from $S(\boldsymbol{x})$ (Fig. 3).

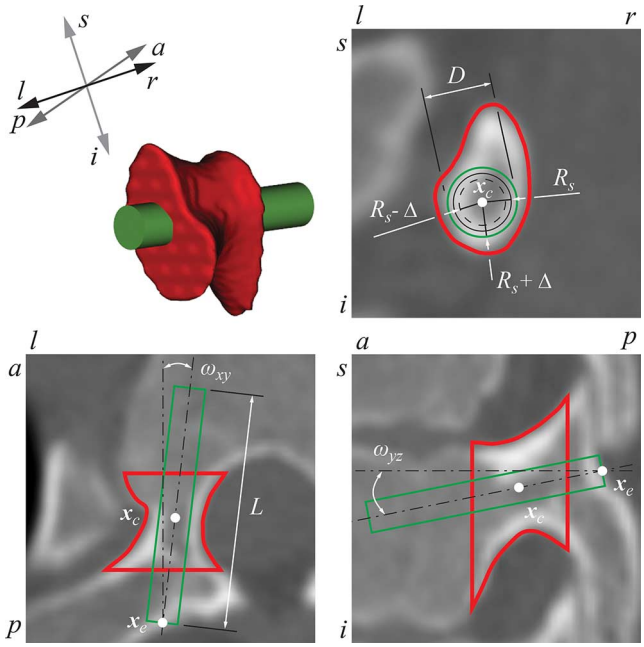

Fig. 3. The pedicle screw placement plan is defined by the screw size with major diameter D and length L, and insertion trajectory with entry point $\boldsymbol{x}_e$ and inclination $\boldsymbol{\omega} = (\omega_{yz}, \omega_{xy})$ (R_s is the screw pitch radius, 2Δ is the span around the screw thread, $\boldsymbol{x}_c$ is the pedicle crossing point). (l-left, r-right, a-anterior, p-posterior, s-superior, i-inferior).

2. The *pedicle screw insertion trajectory* reflects the pose of the screw in 3D and is represented by the screw entry point $\boldsymbol{x}_e = (x_e, y_e, z_e)$ and screw inclination $\boldsymbol{\omega} = (\omega_{yz}, \omega_{xy})$ (Fig. 3). The entry point $\boldsymbol{x}_e$ is defined as the most posterior point on the longitudinal axis of the screw at the transition between bony structures and soft tissues, while inclination $\boldsymbol{\omega}$ is defined by projecting the screw rotation angles $\boldsymbol{\alpha}_s \in \mathcal{R}_S$ onto the sagittal yz-plane (angle ω_{yz}) and onto the axial xy-plane (angle ω_{xy}). The inclination in the coronal xz-plane is not relevant, as it represents the rotation of the circular cylinder about its longitudinal axis.

The extracted parameters $\mathcal{P} = \{D, L, \boldsymbol{x}_e, \boldsymbol{\omega}\}$ represent the pedicle screw placement plan, as they uniquely define the shape (i.e., diameter and length) and pose (i.e., position and rotation) of the pedicle screw in the 3D image for the observed pedicle and the corresponding vertebral body.

III. Experiments and Results

A. Patient Database

The proposed method was evaluated on 11 patients (7 males and 4 females; mean age 17.9 years; range 12–34 years) with adolescent idiopathic scoliosis (9 patients) and degenerative disc disorder (2 patients) in the thoracic spine that underwent CT image acquisition (GE LightSpeed VCT scanner; pixel size 0.25–0.38 mm; slice thickness 0.6 mm) because they were appointed for pedicle screw placement surgery. Preoperative surgery planning was performed by a spine surgeon, who was experienced with the dedicated computer software for 3D image visualization and pedicle screw manipulation that he used to manually plan the size and insertion trajectory of 81 pedicle screws in the acquired CT images between vertebral levels T2 and T12. Basing on these manually defined preoperative plans, patient-specific drill guides were manufactured and physically laid over the exposed part of the spine during surgery, and then pedicle screws with predefined sizes were placed through these guides defining their insertion trajectory.

B. Implementation Framework

The proposed method was implemented in C++ and executed on a personal computer (Intel Core i7 at 3.2 GHz) with 32 GB of memory and graphics processing unit (GPU) acceleration (Nvidia GeForce GTX 760 with CUDA). The implementation consisted of three initialization and alignment phases (Fig. 4), i.e., (1) for 3D vertebral body models, (2) for 3D pedicle models, and (3) for 3D pedicle screw models, which are described in detail in the following subsections. In each phase, the covariance matrix adaptation evolution strategy (CMA-ES) algorithm [26] was applied to maximize the corresponding optimization criterion [(18) and (22)], with $\lambda = 40n$ candidate samples per maximization iteration (n is the number of maximization parameters).

1) Initialization and Alignment of 3D Vertebral Body Models: For each observed vertebral body, the corresponding 3D vertebral body model $V(\boldsymbol{x})$ was obtained through incremental initialization and alignment steps [18]. An elliptical cylinder $V_{init}(\boldsymbol{x})$ was initialized at a manually placed point $\boldsymbol{x}_v$ close to the vertebral body center with rotation of $\boldsymbol{\alpha}_v = (0, 0, 0)$, and size of $2A_v = 30$ mm, $2B_v = 24$ mm and $2H_v = 20$ mm [(2) and (3)] corresponding to the mean size of lower thoracic vertebral bodies [27]. The 3D model was aligned to the vertebral body in the CT image, reinitialized with $(m_l, \sigma_l, \varphi_l) = (0.3, \pi/4, -\pi/4)$, $(m_r, \sigma_r, \varphi_r) = (0.3, \pi/4, \pi/4)$, $(m_f, \sigma_f, \varphi_f) = (0.3, \pi/4, 0)$ and $(m_a, \sigma_a, \varphi_a) = (0.3, \pi/4, \pi)$ that deformed its elliptical cross-section into a more detailed representation of the vertebral body, and then again aligned to the vertebral body in the CT image (4). Finally, the 3D model was reinitialized with $(c_{wa}, c_{wf}) = (0.1, 0.05)$ for the concavity of the vertebral body wall (5), $c_{es} = c_{ei} = 0.1$ for the concavity (6) and $(s_{es}, \psi_{es}) = (s_{ei}, \psi_{ei}) = (0, 0)$ for the inclination of vertebral endplates [(7) and (8)], and $t_{vbs} = t_{vbt} = 0$ for the increasing size and torsion of the vertebral body (9). The reported initialization values for the 3D vertebral body model were obtained by averaging the corresponding manually defined parameters on a selected number of representative vertebrae. The final alignment consisted of optimizing 31 parameters of the composite transformation $\mathcal{R}_V \circ \mathcal{T}_V$ through maximization of the similarity criterion $\mathcal{S}$ [(17) and (18)], i.e., 25 parameters of transformation $\mathcal{T}_V$ that deformed $V_{init}(\boldsymbol{x})$ into $V_{def}(\boldsymbol{x}) = \mathcal{T}_V(V_{init}(\boldsymbol{x}))$ and six parameters of rigid transformation $\mathcal{R}_V$ that transformed $V_{def}(\boldsymbol{x})$ into $V(\boldsymbol{x}) = \mathcal{R}_V(V_{def}(\boldsymbol{x}))$.

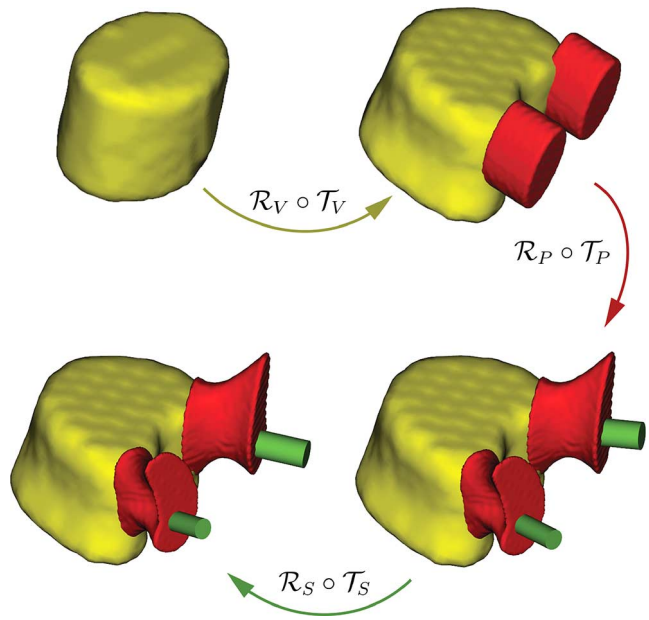

Fig. 4. Transformation $\mathcal{R}_V \circ \mathcal{T}_V$ deforms and aligns the 3D vertebral body model to represent the vertebral body. Similarly, the 3D pedicle model (shown for the left and right pedicle) is deformed and aligned by transformation $\mathcal{R}_P \circ \mathcal{T}_P$ to represent the pedicle. Transformation $\mathcal{R}_S \circ \mathcal{T}_S$ is finally used to obtain the 3D pedicle screw model, which defines the pedicle screw size and insertion trajectory.

2) Initialization and Alignment of 3D Pedicle Models: For each observed pedicle, the corresponding 3D pedicle model $P(\boldsymbol{x})$ was also obtained through incremental initialization and alignment steps. An elliptical cylinder $P_{init}(\boldsymbol{x})$ was first initialized at location $\boldsymbol{x}_p$ (obtained from the final 3D vertebral body model $V(\boldsymbol{x})$, i.e., from parameters $(m_l, \sigma_l, \varphi_l)$ or $(m_r, \sigma_r, \varphi_r)$ representing the location of the left or right pedicle, respectively) with rotation of $\boldsymbol{\alpha}_p = \boldsymbol{\alpha}_v$ corresponding

to the final rotation of $V(\boldsymbol{x})$, and size of $2A_p = 12$ mm, $2B_p = 6$ mm and $2L_p = 10$ mm [(10) and (11)] corresponding to the mean size of lower thoracic pedicles [28]. Additional deformations were initialized as $(c_{ws}, y_{ws}, w_{ws}) = (0.5, 0, L_p)$, $(c_{wi}, y_{wi}, w_{wi}) = (0.5, 0, L_p)$, $(c_{wl}, y_{wl}, w_{wl}) = (0.5, 0, L_p)$ and $(c_{wr}, y_{wr}, w_{wr}) = (0.5, 0, L_p)$ for the concavity of the pedicle wall (12), $c_{lr} = c_{si} = 0$ for the kidney shape and $t_{tp} = 0$ for the torsion of the pedicle [(15) and (16)]. The 3D model was aligned to the pedicle in the CT image, and then reinitialized with $m_{sa} = m_{sp} = m_{ia} = m_{ip} = m_{la} = m_{lp} = m_{ra} = m_{rp} = 0$ for pedicle tails (13) and $(m_{td}, w_{td}, \beta_{td}, \varphi_{td}, \sigma_{td}, y_{td}) = (0, \pi/4, 8, \pm\pi/2, L_p, 0)$ for the teardrop shape of the pedicle, where $\varphi_{td} = -\pi/2$ or $\varphi_{td} = +\pi/2$ when the left or right pedicle was observed, respectively (14). Similarly as for the 3D vertebral body model, the reported initialization values for the 3D pedicle model were obtained by averaging the corresponding manually defined parameters on a selected number of representative vertebrae. The final alignment consisted of optimizing 38 parameters of the composite transformation $\mathcal{R}_P \circ \mathcal{T}_P$ through maximization of the similarity criterion $\mathcal{S}$ [(17) and (18)], i.e., 32 parameters of transformation $\mathcal{T}_P$ that deformed $P_{init}(\boldsymbol{x})$ into $P_{def}(\boldsymbol{x}) = \mathcal{T}_P\left(P_{init}(\boldsymbol{x})\right)$ and six parameters of rigid transformation $\mathcal{R}_P$ that transformed $P_{def}(\boldsymbol{x})$ into $P(\boldsymbol{x}) = \mathcal{R}_P\left(P_{def}(\boldsymbol{x})\right)$.

3) Initialization and Alignment of 3D Pedicle Screw Models: The 3D pedicle screw model $S(\boldsymbol{x})$ was initialized as a circular cylinder $S_{init}(\boldsymbol{x})$ at location $\boldsymbol{x}_s$ (obtained from the final 3D pedicle model $P(\boldsymbol{x})$ and the final 3D vertebral body model $V(\boldsymbol{x})$, i.e., along the longitudinal axis of $P(\boldsymbol{x})$ and by considering the size of $V(\boldsymbol{x})$) with rotation of $\boldsymbol{\alpha}_s = \boldsymbol{\alpha}_p$ corresponding to the final rotation of $P(\boldsymbol{x})$, and size of R_s and L_s defined according to $P(\boldsymbol{x})$ and $V(\boldsymbol{x})$ (19). As pedicle screws larger than 80% of the pedicle radius can cause plastic deformations of the pedicle [29], the initial radius R_s of the pedicle screw was set to 70% [13] of the minimal osculating circle to the surface of $P(\boldsymbol{x})$ along its longitudinal axis, i.e., where the pedicle was the narrowest. On the other hand, pedicle screws that penetrate into the vertebral body for more than 80% of its size in the anterior-to-posterior direction proved to represent a risk of anterior vertebral body wall breakthrough that may result in serious vascular complications [30]. The initial length $2L_s$ of the pedicle screw was therefore computed as the distance along the longitudinal axis of $P(\boldsymbol{x})$ between the point in the anterior part of $V(\boldsymbol{x})$ representing 80% [2] of its corresponding size and the point in the posterior part of the vertebra at the transition between bony structures and soft tissues. A safety margin of $d_s = 0.5$ mm [31] was finally applied to shrink $P(\boldsymbol{x})$ into $P'(\boldsymbol{x})$ to prevent eventual pedicle wall breakthroughs and screw locations on the pedicle surface boundary. The final alignment of the 3D pedicle screw model to vertebral structures in the CT image consisted of optimizing eight parameters of the composite transformation $\mathcal{R}_S \circ \mathcal{T}_S$ through maximization of the normalized fastening strength $\mathcal{F}$ [(20) and (22)], i.e., two parameters of transformation $\mathcal{T}_S$ that deformed $S_{init}(\boldsymbol{x})$ into $S_{def}(\boldsymbol{x}) = \mathcal{T}_S\left(S_{init}(\boldsymbol{x})\right)$ and six parameters of rigid transformation $\mathcal{R}_S$ that transformed $S_{def}(\boldsymbol{x})$ into $S(\boldsymbol{x}) = \mathcal{R}_S\left(S_{def}(\boldsymbol{x})\right)$. The span around the screw thread was set to $\Delta = 0.2R_s$, meaning that 20% of the screw pitch radius was used to obtain its minor and major radii, which is in accordance with the guidelines for pedicle screw design [32].

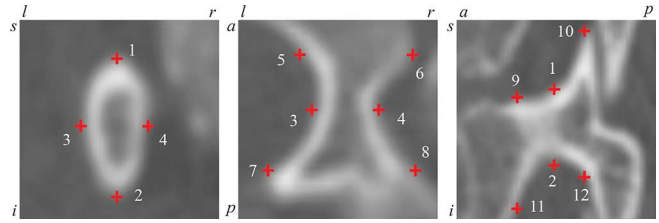

Fig. 5. The ground truth 3D shape and pose of each pedicle were obtained from 12 distinctive anatomical points, identified from cross-sections in the 3D coordinate system of the pedicle that passed through its mid-point. (l-left, r-right, a-anterior, p-posterior, s-superior, i-inferior).

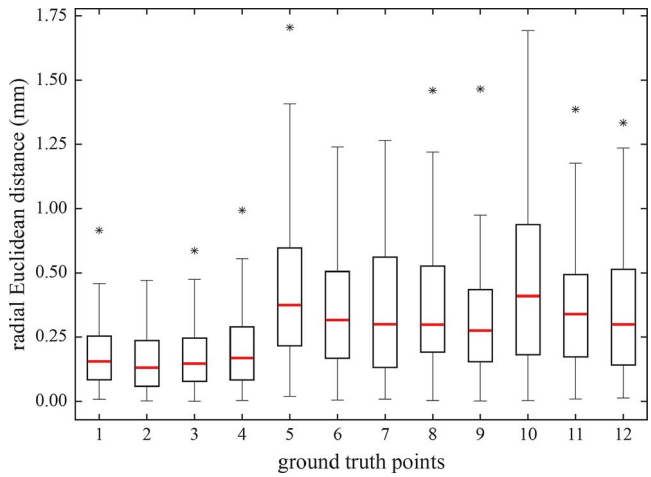

Fig. 6. The box-whisker diagram of distances between the obtained 3D pedicle models and pedicle ground truth points (points are labeled according to Fig. 5; asterisks represent locations of the largest outliers).

C. Results

By analyzing existing manually defined preoperative plans for pedicle screw placement of the studied 11 patients, vertebral bodies and pedicles of interest were identified in corresponding CT images and represented with the proposed 3D vertebral body models and 3D pedicle models, respectively. Ground truth shape and pose of the observed vertebral structures were defined by manually placing 16 distinctive anatomical points on each vertebral body [18] and 12 on each pedicle (Fig. 5), with an estimated reliability of 0.85 ± 0.66 mm for vertebral bodies and 0.68 ± 0.53 mm for pedicles in terms of mean absolute difference (MAD) and corresponding standard deviation (SD), determined from two independently placed sets of anatomical points. For the purpose of quantitative evaluation of the proposed modeling approach, the radial Euclidean distance was measured between each ground truth point and the corresponding 3D model surface point along the line connecting the ground truth point and the 3D model center point. In terms of MAD and corresponding SD of the radial Euclidean distance, the resulting modeling accuracy was 0.39 ± 0.31 mm (range of the mean: 0.23–0.67 mm) for 62 vertebral bodies of interest and 0.31 ± 0.25 mm (range of the mean: 0.16–0.50 mm) for 81 pedicles of interest (Fig. 6). A 3D pedicle screw model was then

TABLE I
COMPARISON BETWEEN AUTOMATICALLY OBTAINED AND MANUALLY DEFINED PLANS FOR PEDICLE SCREW PLACEMENT IN TERMS OF MEAN ABSOLUTE DIFFERENCE (MAD) AND CORRESPONDING STANDARD DEVIATION (SD)

Vertebral level		T2	T3	T4	T5	T6	T7	T8	T9	T10	T11	T12	**All**
No. of screws		2	3	1	3	5	11	10	13	14	8	4	**74**
Screw size													
diameter D	MAD	0.4	0.7	0.2	0.6	0.5	0.4	0.4	0.4	0.6	0.2	0.4	**0.4**
(mm)	SD	0.0	0.2	0.0	0.7	0.4	0.3	0.3	0.3	0.5	0.4	0.5	**0.4**
length L	MAD	3.5	5.0	0.0	6.7	5.0	6.3	5.8	5.3	4.6	7.1	11.5	**5.8**
(mm)	SD	2.1	3.6	0.0	4.7	2.5	4.1	5.5	4.5	2.5	4.1	5.4	**4.2**
Screw insertion trajectory													
pedicle crossing	MAD	1.6	1.3	0.7	1.6	2.0	1.9	1.8	2.0	2.1	2.3	2.9	**2.0**
point $\boldsymbol{x}_c$ (mm)	SD	1.7	0.9	0.0	1.7	1.4	1.7	1.3	1.4	1.3	1.3	1.9	**1.4**
sagittal inclination	MAD	3.4	5.2	1.2	2.6	10.7	7.6	9.1	7.6	11.6	7.3	11.9	**8.5**
angle ω_{yz} (°)	SD	3.8	3.8	0.0	1.4	6.5	5.8	6.4	7.5	8.2	4.3	9.4	**6.8**
axial inclination	MAD	4.5	9.4	6.6	7.1	9.1	4.5	5.6	6.4	6.8	10.2	4.7	**6.7**
angle ω_{xy} (°)	SD	2.4	5.1	0.0	5.9	5.8	3.4	3.7	4.4	3.2	6.4	3.4	**4.4**
Screw planning													
normalized fastening	MAD	12	45	18	51	73	51	58	43	47	31	41	**47**
strength $\mathcal{F}$ (%)	SD	14	21	0	5	43	33	27	13	27	14	19	**26**

automatically defined for each pedicle of interest, and modeling agreement was evaluated by comparing the obtained 3D model parameters to manually defined preoperative plans for pedicle screw placement. For seven pedicle screws, the corresponding pedicle was too narrow (width $\sim$ 3 mm) to fit a screw with sufficient mechanical strength (diameter $>$ 2 mm). For the remaining 74 pedicle screws, the resulting modeling agreement in terms of MAD and corresponding SD was 0.4 ± 0.4 mm for diameter D and 5.8 ± 4.2 mm for length L that define the pedicle screw size, and 2.0 ± 1.4 mm for pedicle crossing point $\boldsymbol{x}_c$ (i.e., the point at the intersection of the longitudinal screw axis with the plane of the minimal osculating circle of the pedicle), $8.5 \pm 6.8°$ for sagittal inclination angle ω_{yz} and $6.7 \pm 4.4°$ for axial inclination angle ω_{xy} that define the pedicle screw insertion trajectory. The corresponding difference in the normalized fastening strength $\mathcal{F}$ was $47 \pm 26\%$, which was before comparison standardized against the mean and SD of manually defined preoperative plans to remove the bias in the appearance of bony structures across different patients. In terms of $\mathcal{F}$, an increase of $48 \pm 26\%$ was observed for 73 pedicle screws (99%), while a decrease of $2 \pm 0\%$ was observed for the remaining pedicle screw (1%). Overall, a statistically significant difference ($p < 0.01$) in $\mathcal{F}$ was observed between automatically obtained and manually defined plans for pedicle screw placement. Detailed results for each individual vertebral level are presented in Table I, and examples of pedicle screw placement plans are shown in Fig. 7. According to preoperative pedicle screw placement plans constructed by a spine surgeon, the manually defined pedicle screw sizes ranged between 4.0 and 5.5 mm with a step of 0.5 mm for screw diameter D (Fig. 8(a)), and between 25 and 55 mm with a step of 5 mm for screw length L (Fig. 8(b)), which is common in clinical practice. In comparison to manually defined plans, the automatically obtained pedicle screw placement plans resulted, on average, in screws of somewhat smaller diameter and shorter length (Fig. 8). However, the distribution of the resulting differences was sparse, which is reflected in the corresponding correlation coefficient of 0.60 for screw diameter D

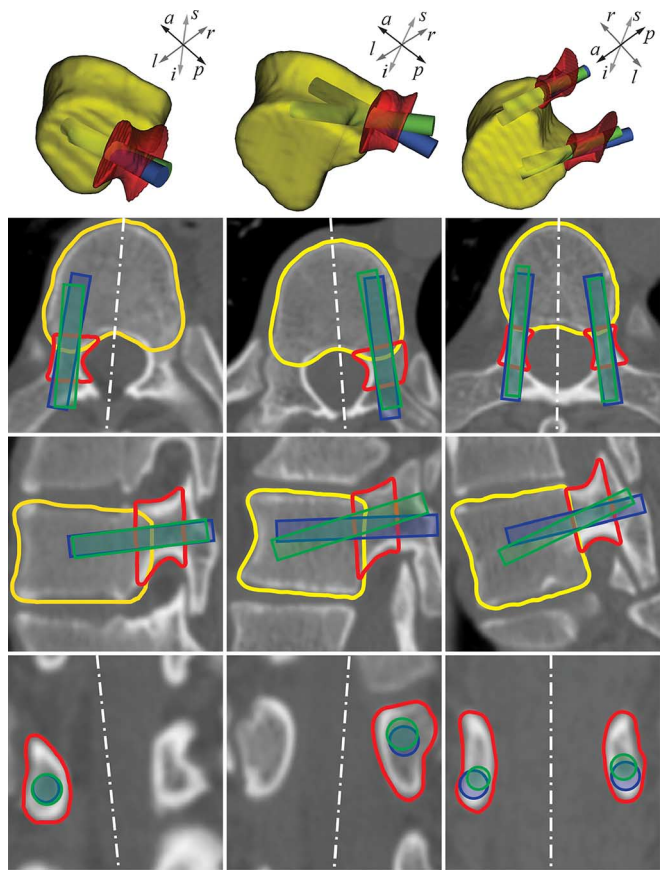

Fig. 7. Visual comparison of automatically obtained (green color) and manually defined (blue color) pedicle screw placement plans for three different patients with adolescent idiopathic scoliosis (first two columns on left) and degenerative disc disease (column on right), shown from top to bottom in a three-dimensional view, and in selected axial, sagittal and coronal views. (l-left, r-right, a-anterior, p-posterior, s-superior, i-inferior).

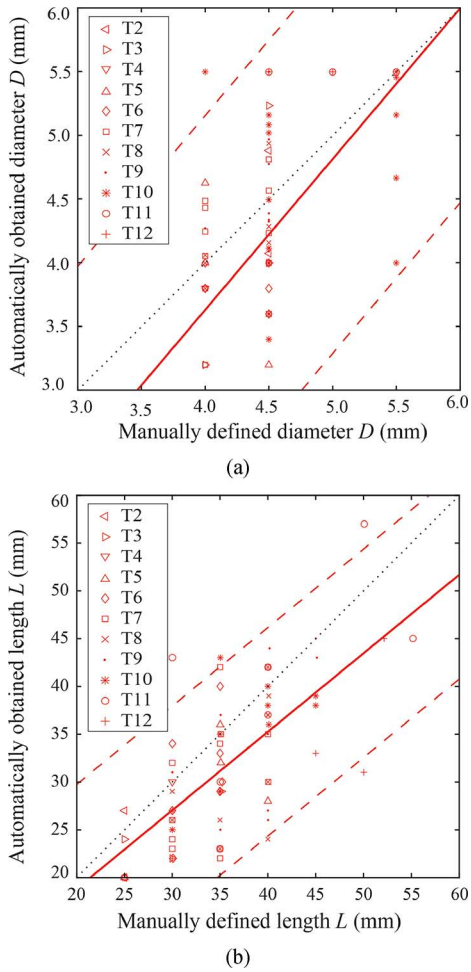

Fig. 8. Scatter plots of the difference between manually defined and automatically obtained pedicle screw size for (a) screw diameter D and (b) screw length L. The line of equality is in dotted black, the line of best fit in solid red, and the upper and lower limits of the 95% confidence interval in dashed red.

and 0.69 for screw length L. Nevertheless, the automatically obtained pedicle screw diameters and lengths are in accordance with the criteria reported in Section III-B3, and can be furthermore rounded with respect to screw sizes that are currently used in clinical practice.

IV. Discussion and Conclusion

Although the concept of optimal surgery planning for pedicle screw placement was addressed in several studies [13], [14], [23], the definition of optimality is not clearly defined. Optimal pedicle screw sizes and insertion trajectories are not only those that do not cause injuries by intraoperative vertebral body or pedicle wall breakthrough, but in a more broader sense those that do not result in injuries, complications, functional disability and/or pain for the patient in the short- and long-term postoperative periods. As objective prediction and quantification of long-term effects is difficult, it is not clear what exactly optimal pedicle screw size and insertion trajectory are. Nevertheless it is important to strive for such an operative plan that will provide optimal results according to selected criteria based on current advances in biomechanical and clinical knowledge. In this paper, we described a novel automated method for computer-assisted preoperative planning of the thoracic pedicle screw size and insertion trajectory that combines both vertebral geometrical and structural properties for a fast and reliable planning of pedicle screw placement surgery.

The criteria adopted for evaluating vertebral geometrical properties were obtained by parametric modeling of vertebral bodies and pedicles in 3D. In comparison to statistical shape modeling with active shape/appearance or articulated deformable models [33]–[35], the applied parametric modeling generalizes the description of vertebral anatomy and therefore suppresses local anatomical deformations (e.g., Schmorl's nodes). However, to capture such local deformations by statistical shape modeling, they would have to appear frequently in a training database that would have to be (manually) annotated, but could be nevertheless masked by non-deformed and normal cases. Moreover, a large number of eigenshapes representing modes of shape variations would be required to capture such deformations. On the other hand, besides the fact that the applied parametric modeling does not require a training database and corresponding manual annotations, known local anatomical deformations could still be modeled at expected locations by introducing parameters describing their shape (e.g., Schmorl's nodes could be modeled by searching for protrusions along the obtained vertebral endplates), which however depends on the occurrence of such deformations in the given patient database. For the given patient database, the applied parametric approach resulted in relatively high modeling accuracy of every of the 62 observed vertebral bodies and 81 observed pedicles, which can be in part attributed to the application of the CMA-ES optimization algorithm [26] for 3D model alignment, which has, in comparison to the downhill simplex algorithm [18], a global search behavior. Although the number of iterations rapidly increases with the number of candidate samples per iteration [26], we implemented the proposed method on GPU to decrease the computation time that amounted to around 2 min for the determination of each 3D vertebral body or pedicle model, which can be, however, performed completely off-line. Although each 3D vertebral body model requires initialization in the form of a manually placed point close to the vertebral body center, the resulting modeling accuracy is not considerably affected, as a successful model alignment (i.e., convergence) can be achieved even with the downhill simplex algorithm if this point is up to 10 mm from the vertebral body center [18]. The high modeling accuracy is especially important in the case of pedicles due to their small size when compared to vertebral bodies. Moreover, from Fig. 6 it can be observed that the pedicle modeling accuracy is higher for the pedicle wall at its narrowest part (i.e., points 1–4 in Fig. 5) than for pedicle tails (i.e., points 5–12 in Fig. 5). From the perspective of pedicle screw placement, the narrowest part of the pedicle is also its most important part, as pedicle wall breakthrough usually occurs around this region, and we used it to determine the minimal osculating circle of the pedicle containing the screw. According to the most widely accepted grading system in clinical practice [12], the acceptable safe zone for screws is defined for pedicle wall breaches of up to 2 mm. Considering that the obtained pedicle modeling accuracy is around 0.5 mm,

a maximal error of 1.5 mm is still allowed when applying image-guided and/or navigation techniques for pedicle screw placement. Although the pedicle screw size and insertion trajectory could be determined without modeling of vertebral structures, parametric modeling in 3D enables extraction of vertebral body and pedicle morphology that provided crucial information related to the screw size and insertion trajectory, e.g., the size of the vertebral body and pedicle, and the virtual plane of vertebral symmetry (Section II-B2). Moreover, it enables vertebral body and pedicle segmentation [36], [37] and labeling [38], [39], which can be used for enhanced 3D visualization, e.g., by overlaying 3D models on the segmented CT images [40], [41]. Knowledge of vertebral morphology and segmentation in 3D combined with enhanced vertebral visualization in 3D may help the surgeon to preoperatively gain a better mental conceptualization and reconstruction of the 3D spinal anatomy.

For evaluating vertebral structural properties, we adopted a criterion based on CT image intensities representing the pedicle screw fastening strength, which proved to be related to the underlying BMD and further to the screw pull-out strength [2], [23], [24], which is especially important for patients with osteoporosis [42]. However, we took into account only the volume around the screw thread that actually contributes to the fastening strength, applied a safety margin around the pedicle surface to prevent eventual pedicle wall breakthroughs, weighted the underlying image intensities within this volume to account for the trade-off between BMD of the cortical and trabecular bone, and normalized the result with the screw thread volume to eliminate the influence of the pedicle screw size in order to obtain a criterion with a clearly distinctive and oriented maximum (Fig. 9) that was used for aligning 3D pedicle screw models to vertebral structures in CT images. If required by the spine surgeon or imposed by the patient-specific anatomy, the applied safety margin around the pedicle surface can be defined manually, and even differently at the medial and lateral pedicle wall to account for the higher risks and larger complications related to medial in comparison to lateral pedicle wall breakthroughs. In the current implementation, however, the safety margin that is in clinical practice also termed as the bony bridge was set to $d_s = 0.5\,\mathrm{mm}$ [31]. The proposed method was evaluated on 81 pedicles and the automatically obtained plans for pedicle screw placement were compared to those that were manually defined by a spine surgeon, resulting in a relatively high agreement between the two approaches, where an increase in the screw fastening strength in favor of the automated approach was observed in 99% of the cases. It has to be noted that by such comparison, we did not aim to obtain an as close as possible match between the two approaches, because the concept of optimal surgery planning for pedicle screw placement is, as mentioned above, not clearly defined. The purpose of comparison was to show that the automatically defined pedicle screw size and insertion trajectory correspond to the maximal available fastening strength, and therefore represent an adequate choice for the operative plan from the biomechanical as well as clinical perspective. The computation time for the determination of each 3D pedicle screw model amounted to around 20 sec, which can be performed completely off-line but eventually also on-line if the spine surgeon would decide to manually select the screw size or insertion trajectory while revising the proposed operative plan.

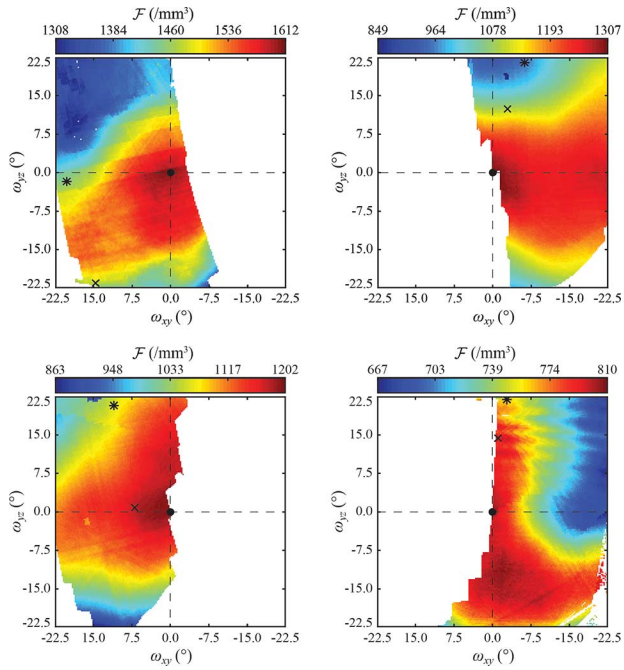

Fig. 9. Distribution maps of the normalized fastening strength $\mathcal{F}$ for selected screws through the left pedicle (left column) and right pedicle (right column), generated by systematically modifying screw sagittal ω_{yz} and axial ω_{xy} inclinations from automatically obtained insertion trajectories while keeping screws completely within the observed pedicles and vertebral bodies. Black circles, asterisks and crosses represent, respectively, corresponding automatically obtained, manually defined and anatomical (i.e., along the longitudinal axis of the pedicle) insertion trajectories. White areas represent harmful insertion trajectories that resulted in screws not completely within the observed pedicles and vertebral bodies.

Pedicle morphometry is of utmost importance for a safe pedicle screw placement, and was therefore the topic of several studies that measured pedicle dimensions manually with a digital caliper from human cadavers [4], [43] or with virtual measurement tools in 2D image cross-sections [23], [28]. The method proposed in this paper extracts the 3D shape of the pedicle in the form of a novel 3D parametric model, which enables direct pedicle morphometry measurements, as each 3D pedicle model parameter is associated with a specific shape characteristic. The extracted pedicle morphometry is then used for computer-assisted preoperative planning of the screw size and insertion trajectory for pedicle screw placement surgery.

ACKNOWLEDGMENT

The authors thank Ekliptik d.o.o., Slovenia, for providing images and manual preoperative pedicle screw placement plans.

REFERENCES

[1] C. S. Lee *et al.*, "A novel method of screw placement for extremely small thoracic pedicles in scoliosis," *Spine*, vol. 36, no. 16, pp. E1112–E1116, Jul. 2011.

[2] R. A. Lehman *et al.*, "Straight-forward versus anatomic trajectory technique of thoracic pedicle screw fixation: A biomechanical analysis," *Spine*, vol. 28, no. 18, pp. 2058–2065, Sep. 2003.

[3] T. Vrtovec, F. Pernuš, and B. Likar, "Variability of manual and computerized methods for measuring coronal vertebral inclination in computed tomography images," *Image Anal. Stereol.*, Jun. 2015.

[4] C. C. Yu *et al.*, "Lower thoracic pedicle morphometry: Male, taller, and heavier specimens have bigger pedicles," *Spine*, vol. 40, no. 6, pp. E323–E331, Mar. 2015.

[5] N.-F. Tian *et al.*, "Pedicle screw insertion accuracy with different assisted methods: A systematic review and meta-analysis of comparative studies," *Eur. Spine J.*, vol. 20, no. 6, pp. 846–859, Sep. 2010.

[6] A. Manbachi, R. S. Cobbold, and H. J. Ginsberg, "Guided pedicle screw insertion: Techniques and training," *Spine J.*, vol. 14, no. 1, pp. 165–179, Jan. 2014.

[7] M. Gstoettner, R. Lechner, B. Glodny, M. Thaler, and C. M. Bach, "Inter- and intraobserver reliability assessment of computed tomographic 3D measurement of pedicles in scoliosis and size matching with pedicle screws," *Eur. Spine J.*, vol. 20, no. 10, pp. 1771–1779, Jul. 2011.

[8] A. Uneri *et al.*, "Known-component 3D–2D registration for quality assurance of spine surgery pedicle screw placement," *Phys. Med. Biol.*, vol. 60, no. 20, pp. 8007–8024, Sep. 2015.

[9] C. J. Kleck *et al.*, "A new 3-dimensional method for measuring precision in surgical navigation and methods to optimize navigation accuracy," *Eur. Spine J.*, Sep. 2015.

[10] P. Markelj, D. Tomaževič, B. Likar, and F. Pernuš, "A review of 3D/2D registration methods for image-guided interventions," *Med. Image Anal.*, vol. 16, no. 3, pp. 642–661, Apr. 2012.

[11] Y. R. Rampersaud, D. A. Simon, and K. T. Foley, "Accuracy requirements for image-guided spinal pedicle screw placement," *Spine*, vol. 26, no. 4, pp. 352–359, Feb. 2001.

[12] A. A. Aoude *et al.*, "Methods to determine pedicle screw placement accuracy in spine surgery: A systematic review," *Eur. Spine J.*, vol. 24, no. 5, pp. 990–1004, May 2015.

[13] J. Lee, S. Kim, Y. S. Kim, and W. K. Chung, "Optimal surgical planning guidance for lumbar spinal fusion considering operational safety and vertebra-screw interface strength: Optimal surgical planning guidance for lumbar spinal fusion," *Int. J. Med. Robot. Comput. Assist. Surg.*, vol. 8, no. 3, pp. 261–272, Sep. 2012.

[14] R. Wicker and B. Tedla, "Automatic determination of pedicle screw size, length, and trajectory from patient data," in *Proc. 26th Annu. Int. Conf. IEEE Eng. Med. Biol. Soc.*, Sep. 2004, pp. 1487–1490.

[15] A. Barr, "Superquadrics and angle-preserving transformations," *IEEE Comput. Graph. Appl.*, vol. 1, no. 1, pp. 11–23, Jan. 1981.

[16] A. Jaklič, A. Leonardis, and F. Solina, *Segmentation and Recovery of Superquadrics*, M. A. Viergever, Ed. New York: Springer, 2000, vol. 20.

[17] R. Korez, B. Likar, F. Pernuš, and T. Vrtovec, "Parametric modeling of the intervertebral disc space in 3D: Application to CT images of the lumbar spine," *Comput. Med. Imag. Graph.*, vol. 38, no. 7, pp. 596–605, Oct. 2014.

[18] D.Štern, B. Likar, F. Pernuš, and T. Vrtovec, "Parametric modelling and segmentation of vertebral bodies in 3D CT and MR spine images," *Phys. Med. Biol.*, vol. 56, no. 23, pp. 7505–7522, Dec. 2011.

[19] M. M. Panjabi, J. D. O'Holleran, J. J. Crisco, III, and R. Kothe, "Complexity of the thoracic spine pedicle anatomy," *Eur. Spine J.*, vol. 6, no. 1, pp. 19–24, 1997.

[20] H. Ma *et al.*, "Generation of flat-top beam with phase-only liquid crystal spatial light modulators," *J. Opt.*, vol. 12, no. 4, p. 045704, Apr. 2010.

[21] D. Comaniciu, V. Ramesh, and P. Meer, "Kernel-based object tracking," *IEEE Trans. Pattern Anal. Mac. Intel.*, vol. 25, no. 5, pp. 564–577, May 2003.

[22] J. R. Chapman *et al.*, "Factors affecting the pullout strength of cancellous bone screws," *J. Biomech. Eng.*, vol. 118, no. 3, pp. 391–398, Aug. 1996.

[23] C. A. Linte, K. E. Augustine, J. J. Camp, R. A. Robb, and D. R. Holmes, III, "Toward virtual modeling and templating for enhanced spine surgery planning," in *Spinal Imag. Image Anal.*, S. Li and J. Yao, Eds. New York: Springer, 2015, vol. 18, Lecture Notes Comput. Vis. Biomechan., pp. 441–467.

[24] J. J. Schreiber, "Hounsfield units for assessing bone mineral sensity and strength: A tool for osteoporosis management," *J. Bone Joint Surg. Am.*, vol. 93, no. 11, pp. 1057–1063, Jun. 2011.

[25] P. E. Chatzistergos, E. A. Magnissalis, and S. K. Kourkoulis, "Numerical simulation of bone screw induced pretension: The cases of under-tapping and conical profile," *Med. Eng. Phys.*, vol. 36, no. 3, pp. 378–386, Mar. 2014.

[26] N. Hansen and A. Ostermeier, "Completely derandomized self-adaptation in evolution strategies," *Evol. Comput.*, vol. 9, no. 2, pp. 159–195, 2001.

[27] Y. Masharawi *et al.*, "Vertebral body shape variation in the thoracic and lumbar spine: Characterization of its asymmetry and wedging," *Clin. Anat.*, vol. 21, no. 1, pp. 46–54, Jan. 2008.

[28] A. R. Vaccaro *et al.*, "Placement of pedicle screws in the thoracic spine, Part I: Morphometric analysis of the thoracic vertebrae," *J. Bone Joint Surg.*, vol. 77, no. 8, pp. 1193–1199, Aug. 1995.

[29] G. R. Misenhimer, R. D. Peek, L. L. Wiltse, S. L. G. Rothman, and E. H. Widell, "Anatomic analysis of pedicle cortical and cancellous diameter as related to screw size," *Spine*, vol. 14, no. 4, pp. 367–372, Apr. 1989.

[30] A. Biyani and H. S. An, "Principles of spinal instrumentation in degenerative disorders of the lumbar spine," in *The Lumbar Spine*, H. N. Herkowitz, J. Dvorak, G. Bell, M. Nordin, and D. Grob, Eds., 3rd ed. Philadelphia, PA: Lippincott Williams Wilkins, 2004, pp. 268–285.

[31] Z. Zhuang *et al.*, "Thoracic pedicle morphometry in different body height population: A three-dimensional study using reformatted computed tomography," *Spine*, vol. 36, no. 24, pp. E1547–E1554, Nov. 2011.

[32] D. A. Baluch *et al.*, "Effect of physiological loads on cortical and traditional pedicle screw fixation," *Spine*, vol. 39, no. 22, pp. E1297–E1302, Oct. 2014.

[33] A. Mastmeyer, K. Engelke, C. Fuchs, and W. A. Kalender, "A hierarchical 3D segmentation method and the definition of vertebral body coordinate systems for QCT of the lumbar spine," *Med. Image Anal.*, vol. 10, no. 4, pp. 560–577, Aug. 2006.

[34] T. Klinder *et al.*, "Automated model-based vertebra detection, identification, and segmentation in CT images," *Med. Image Anal.*, vol. 13, no. 3, pp. 471–482, Jun. 2009.

[35] S. Kadoury, H. Labelle, and N. Paragios, "Spine segmentation in MEDICAL images using manifold embeddings and higher-order MRFs," *IEEE Trans. Med. Imag.*, vol. 32, no. 7, pp. 1227–1238, Jul. 2013.

[36] Z. Wang *et al.*, "Regression segmentation for M^3 spinal images," *IEEE Trans. Med. Imag.*, vol. 34, no. 8, pp. 1640–1648, Aug. 2015.

[37] M. Pereanez *et al.*, "Accurate segmentation of vertebral bodies and processes using statistical shape decomposition and conditional models," *IEEE Trans. Med. Imag.*, vol. 34, no. 8, pp. 1627–1639, Aug. 2015.

[38] Y. Cai, S. Osman, M. Sharma, M. Landis, and S. Li, "Multi-modality vertebra recognition in arbitrary views using 3D deformable hierarchical model," *IEEE Trans. Med. Imag.*, vol. 34, no. 8, pp. 1676–1693, Aug. 2015.

[39] B. De Leener, J. Cohen-Adad, and S. Kadoury, "Automatic segmentation of the spinal cord and spinal canal coupled with vertebral labeling," *IEEE Trans. Med. Imag.*, vol. 34, no. 8, pp. 1705–1718, Aug. 2015.

[40] I. Castro-Mateos *et al.*, "Statistical interspace models (SIMs): Application to robust 3D spine segmentation," *IEEE Trans. Med. Imag.*, vol. 34, no. 8, pp. 1663–1675, Aug. 2015.

[41] R. Korez, B. Ibragimov, B. Likar, F. Pernuš, and T. Vrtovec, "A framework for automated spine and vertebrae interpolation-based detection and model-based segmentation," *IEEE Trans. Med. Imag.*, vol. 34, no. 8, pp. 1649–1662, Aug. 2015.

[42] R. A. Lehman, D. G. Kang, and S. C. Wagner, "Management of osteoporosis in spine surgery," *J. Am. Acad. Orthop. Surg.*, vol. 23, no. 4, pp. 253–263, Apr. 2015.

[43] C. C. Yu, N. S. Bajwa, J. O. Toy, U. M. Ahn, and N. U. Ahn, "Pedicle morphometry of upper thoracic vertebrae: An anatomic study of 503 cadaveric specimens," *Spine*, vol. 39, no. 20, pp. E1201–E1209, Sep. 2014.